Analysis of Inlet Velocity Profiles in Numerical Assessment of Fontan Hemodynamics

Zhenglun Alan Wei[1,§], **Connor Huddleston**[2,§], **Phillip M. Trusty**[1], **Shelly Singh-Gryzbon**[1], **Mark A. Fogel**[3], **Alessandro Veneziani**[4], **Ajit P. Yoganathan**[1,*]

[1]Wallace H. Coulter School of Biomedical Engineering, Georgia Institute of Technology, Atlanta, GA, USA

[2]School of Chemistry and Biochemistry, Georgia Institute of Technology, Atlanta, GA, USA

[3]Department of Cardiology, Children's Hospital of Philadelphia, Philadelphia, PA, USA

[4]Department of Mathematics, Department of Computer Science, Emory University, Atlanta, GA, USA

Abstract

Computational fluid dynamic (CFD) simulations are widely utilized to assess Fontan hemodynamics that are related to long-term complications. No previous studies have systemically investigated the effects of using different inlet velocity profiles in Fontan simulations. This study implements real, patient-specific velocity profiles for numerical assessment of Fontan hemodynamics using CFD simulations. Four additional, artificial velocity profiles were used for comparison: (1) flat, (2) parabolic, (3) Womersley, and (4) parabolic with inlet extensions (to develop flow before entering the TCPC). The differences arising from the five velocity profiles, as well as discrepancies between the real and each of the artificial velocity profiles, were quantified by examining clinically important metrics in TCPC hemodynamics: power loss (PL), viscous dissipation rate (VDR), hepatic flow distribution, and regions of low wall shear stress. Statistically significant differences were observed in PL and VDR between simulations using real and flat velocity profiles, but differences between those using real velocity profiles and the other three artificial profiles did not reach statistical significance. These conclusions suggest that the artificial velocity profiles (2), (3), and (4) are acceptable surrogates for real velocity profiles in Fontan simulations, but parabolic profiles are recommended because of their low computational demands and prevalent applicability.

Keywords

Computational Fluid Dynamics; Fontan Hemodynamics; Inlet Velocity Profiles

---

[*]Correspondence author: Ajit P. Yoganathan, Ph.D., Member National Academy of Engineering, The Wallace H. Coulter Distinguished Faculty Chair in Biomedical Engineering & Regents Professor Assoc. Georgia Institute of Technology, 387 Technology Circle, Suite 232, Atlanta, GA 30313-2412, Tel: 404.894.2849, Fax: 404.385.1268, ajit.yoganathan@bme.gatech.edu.
[§]Dr. Wei and Mr. Huddleston contributed equally to the current work.

1 Introduction

The Fontan procedure is a palliative surgical procedure commonly performed on pediatric patients born with congenital single ventricle heart defects. Such patients often suffer from a critically low oxygen saturation since oxygenated and deoxygenated blood mix in the single ventricle. To alleviate this problem, the standard Fontan procedure reroutes the venous return directly to the pulmonary arteries, creating a total cavopulmonary connection (TCPC) that separates the pulmonary and systemic circulations (separating oxygenated and deoxygenated blood). Though this procedure generally results in favorable short-term outcomes, a single ventricle circulation still performs less efficiently than that of a standard biventricular heart. Many Fontan patients have been known to develop long-term complications after the surgery that have been linked to compromised TCPC hemodynamics[10, 24].

To assess Fontan hemodynamics, computational fluid dynamic (CFD) simulations are often performed on patient-specific TCPC models. These simulations help researchers understand clinically important factors such as power loss (PL), hepatic flow distribution (HFD), and wall shear stress (WSS) in the context of Fontan hemodynamics. PL has been correlated to exercise intolerance which is universal among Fontan patients [9, 34], HFD has been linked to the development of postoperative pulmonary arteriovenous malformations (PAVMs)[15, 22], and recent studies have suggested that abnormal WSS is related to underdevelopment of the pulmonary arteries and the formation of blood clots[11, 36]. The use of patient-specific anatomies further augments the clinical power of CFD simulations and enables the use of surgical planning platforms[16], allowing surgeons to understand the predicted hemodynamics of proposed surgical strategies.

A crucial aspect of the reliability of CFD simulations is the choice of boundary conditions (BCs)[14]. This topic has been extensively investigated[7, 12, 14, 18, 37], as there is generally a gap between the data required for mathematical models and that which is available. Typically, vessel flow rates are available, but the full velocity profiles required by mathematical models are not. Traditionally, a Dirichlet boundary condition with an arbitrary velocity profile is selected to fit the available flow rate. Utilizing a Neumann boundary condition as inflow boundaries is prone to numerical instabilities and requires to be associated with a Dirichlet pressure boundary condition[1, 2, 20]. Unfortunately, patient-specific pressure, which could be obtained by invasive catheterization, is not available from the stand-of-care clinical practice. Two of the most popular choices of Dirichlet inlet BCs for CFD simulations of the cardiovascular system are flat and parabolic velocity profiles. While far from the patient-specific velocity profile obtained from medical imaging, these two profiles are simple to describe, easily adapted to the inflow section, and preserve patient-specific volumetric flow rates. When used in conjunction with patient-specific anatomies, parabolic velocity profiles are believed to provide an acceptable interpretation of the patient's true hemodynamics, e.g., in simulations regarding the carotid bifurcation[4]. However, the parabolic profile is, in fact, the solution of the blood flow equations under steady conditions, ignoring the pulsatile nature of cardiovascular flows. This profile can accommodate pulsatile flows by changing the instantaneous flow rate to fit; however, the mathematical background of this choice is questionable. To overcome this shortcoming, the Womersley profile[35] is often used. This profile is the counterpart to the parabolic solution

derived in a cylindrical domain under pulsatile conditions. The combination of Womersley elementary profiles (referring to a specific frequency) can be used to fit a given periodic, time-varying flow rate in a manner more consistent with pulsatility than the parabolic approach. In order to mitigate the impact of these arbitrary choices on the solution in the region of interest, a common practice is to add cylindrical regions called "flow extensions" at the inlets of the domain, alleviating the effects of the arbitrary choice far from the critical regions of interest[17]. Jansen et al. concluded that Womersley profiles, in comparison to parabolic profiles, result in different wall shear stress magnitudes in cerebral aneurysmal hemodynamics[8]. Similar findings have resulted from numerical modeling of abdominal aortic aneurysms[7] and the thoracic aorta[37]. However, very few studies have investigated the differences in using the aforementioned artificial velocity profiles in comparison with a real, patient-specific velocity profile. In particular, no previous literature has discussed the choice of inlet velocity profiles on the computational assessment of TCPC hemodynamics.

This study directly investigates the effects of these velocity profiles on Fontan hemodynamics with a numerical sensitivity analysis of the aforementioned relevant clinical hemodynamic metrics. CFD simulations were conducted for nine Fontan patients. Inlet BCs were imposed by either a real, patient-specific velocity profile or one of four artificial velocity profiles: (1) flat profile, (2) parabolic profile, (3) Womersley profile, or (4) numerical profile developed by adding extensions to the original inlets of the TCPC. Differences stemming from the use of the different velocity profiles, as well as discrepancies between the use of the real and each of the four artificial profiles, were quantified by comparing the resulting relevant TCPC hemodynamic metrics.

2 Materials and Methods

2.1 Patient Cohort

This study was a retrospective analysis of patient data acquired from the Georgia Tech-Children's Hospital of Philadelphia Fontan database. Nine (n=9) patient datasets were selected based on their cardiac output, pulsatility indices, and Womersley number. Informed consent was obtained, and the protocol was approved by the Georgia Institute of Technology and Children's Hospital of Philadelphia institutional review boards.

2.2 Velocity Segmentation and Anatomical Reconstruction

Phase-contrast magnetic resonance imaging (PC-MRI) data were acquired at the Children's Hospital of Philadelphia. Each scan was taken under breath-held conditions and was electrocardiogram-gated. The inlet and outlet velocities of each patient's TCPC were segmented from the PC-MRI scans using Segment (Medviso AB, Lund, Sweden). From this segmentation, a series of 3D patient-specific velocity profiles in space, as well as volumetric flow waveforms, were obtained for each vessel over the length of the cardiac cycle.

As depicted in Figure 1, the PC-MR segmented flows and patient-specific velocity profiles were interpolated in both time and space in preparation for CFD simulation. The temporal resolution between PC-MR images for all cases was 31.01 ± 4.09 ms, while the pixel size (spatial resolution) for all inlet vessel images was 1.18 ± 0.17 mm $\times$ 1.18 ± 0.17 mm.

However, finer temporal and spatial resolutions are required for accurate transient CFD results. In order to achieve this temporal resolution, the volumetric flow waveform for all vessels was decomposed through a Fast Fourier Transform (FFT) into Fourier coefficients, from which the waveform could be reconstructed to the desired level of temporal accuracy. To increase spatial resolution, the 3D, patient-specific velocity profiles of the inlet vessels were interpolated from the coarse MR grid to the centroids of the CFD mesh.

Cardiac magnetic resonance imaging (MRI) data were acquired at the Children's Hospital of Philadelphia. Each scan was taken under breath-held conditions and was electrocardiogram-gated. The 3D geometry of each patient's TCPC was segmented and reconstructed from the MR scans using 3D Slicer (http://www.slicer.org). Following anatomy segmentation, each 3D TCPC model was smoothed and reconstructed using Geomagic Studio (Geomagic Inc., NC, USA). An in-house MATLAB (R2016b, The Mathworks Inc., Natick, MA) code was used to determine the spatial location and angle at which the PC-MRI scans were acquired, and the inlets and outlets of each model were trimmed with a plane accordingly, as shown in Figure 2. This planar trimming was performed to ensure that the patient-specific inlet velocity profile would be imposed on the reconstructed anatomy at the same spatial orientation/location as the *in vivo* measurements.

2.3   CFD Simulations

3D, pulsatile CFD simulations of blood flow through the TCPC were run using Fluent (v17.0, ANSYS Inc., Canonsburg, PA). A polyhedral mesh with 10 layers of boundary layer mesh (geometric growth ratio = 1.05) was used, and the average diameter of each model's inlet and outlet vessels divided by 50 was employed as the mesh size to ensure grid-independent simulation results[32] (number of computational cells = 1,958,674 ± 696,182). No-slip boundary conditions were imposed on the TCPC wall with the rigid wall assumption. All simulations for a given patient used the same mesh, CFD parameters, and time-varying patient-specific flow ratios between the LPA and RPA derived from PC-MRI. Blood was modeled as a non-Newtonian fluid (with a density $\rho = 1060$ kg/m^3) with Carreau model curve-fitted data from Cheng *et al*.[5] The Carreau model is expressed in

$\eta(\dot{\gamma}) = \eta_\infty + (\eta_0 - \eta_\infty)\left[1 + (\dot{\gamma}\lambda)^2\right]^{\frac{n-1}{2}}$, where $\dot{\gamma}$ is the shear rate, time constant $(\lambda) = 3.34$ (s), power-law index $(n) = 0.3025$, zero shear viscosity $(\eta_0) = 0.06109$ (kg/m-s), and infinite shear viscosity $(\eta_\infty) = 0.003218$ (kg/m-s). No turbulence modeling was used in the simulations of this study because of the relatively low Reynolds numbers, as shown in Table I. The coupled flow model was utilized. Pressure and momentum discretization employed the second-order implicit and third-order MUSCL schemes, respectively. The transient formula was the second-order implicit scheme. Warped-face gradient correction was enabled to enhance the accuracy of gradient calculation in the polyhedral mesh. Time step size was 1E-3 seconds, and convergence criteria were 1E-4.

For each patient-specific geometry, five simulations were run, only varying the inlet velocity profiles. One simulation was run with extensions (of length equal to 10 times the vessel diameter) on the inlet vessels and parabolic profiles implemented at the ends of the extensions as BCs. This case allowed the flow to develop before entering the TCPC and is

therefore referred to as the case with "*extension-developed*" velocity profiles throughout the rest of this study. The other four simulations did not include any extensions on the inlets but directly implemented either *flat, parabolic, Womersley*, or *real, patient-specific* velocity profiles on the original inlet vessels. The first three profiles were calculated from the patient-specific volumetric flow waveform. Since the cross-sections of most TCPC inlet vessels were very close to circular in this study, a direct implementation of parabolic or Womersley profiles resulted in less than 5% error in flow rate. The numerical velocity profile was regulated by adding any discrepancy in flow rate to all computational cells of the inlet surface in simulations based on the ratio of the local flux through the cell face to the global flux of the inlet surface. This procedure ensured that the only difference between simulations using different velocity profiles was the spatial velocity distribution. The parabolic profile was implemented using a user-defined function (UDF) in ANSYS Fluent. Both the Womersley and real velocity profiles were constructed with an in-house MATLAB code based on the computational mesh and imported to the CFD simulation via UDF. The Womersley profile followed (Eqs. 1) & (2):

$$Q(t) \approx \sum_{n=0}^{N} B_n e^{in\omega t} \tag{1}$$

$$U(r,t) = \frac{2B_0}{\pi R^2}\left[1 - \left(\frac{r}{R}\right)^2\right] + \sum_{n=1}^{N}\left\{\frac{B_n}{\pi R^2}\left[\frac{1 - J_0\left(\alpha_n\frac{r}{R}i^{3/2}\right)\big/J_0\left(\alpha_n i^{3/2}\right)}{1 - 2J_1\left(\alpha_n i^{3/2}\right)\big/\alpha_n i^{3/2}J_0\left(\alpha_n i^{3/2}\right)}\right]\right\}e^{in\omega t} \tag{2}$$

where ω is the angular frequency of the temporal velocity waveform and R is the radius of the vessel calculated by using $(\text{Area}/\pi)^{0.5}$. B_n are Fourier coefficients that decompose a time-varying flow rate $Q(t)$, and $\alpha_n = R\sqrt{\rho(n\omega)/\mu}$, where $\mu = 0.0034$ Pa-s. J_0 and J_1 are Bessel functions of the first kind of order 0 and 1, respectively.

2.4 Quantification of Discrepancy between Velocity Profiles

The intrinsic discrepancies between the parabolic, Womersley, or extension-developed velocity profile and the real patient-specific velocity profile were quantified by their root-mean-square deviation (RMSD):

$$\text{RMSD}(t) = \sqrt{\left.\int_{Surface}\left(Y_i(t) - y_i(t)\right)^2 dA\right|Area} \tag{3}$$

where Y_i is a velocity of the actual patient-specific profile and y_i is the corresponding velocity of either the flat, parabolic, Womersley, or extension-developed profile. This RMSD was normalized by the ratio of the mean volumetric flow rate through the vessel at a given time to the area of the vessel:

$$\text{nRMSD}(t) = \frac{\text{RMSD}(t)}{Q(t)/Area} \tag{4}$$

The resulting nRMSD was then averaged over a cardiac cycle to obtain a time-averaged value, $\text{nRMSD}_{\text{avg}}$, between the flat, parabolic, Womersley, or extension-developed and real velocity profiles. This analysis was intended to directly compare the discrepancy between the profiles and understand error propagation from velocity segmentation to simulated Fontan hemodynamics.

2.5 Hemodynamic Metrics

In this study, clinically relevant hemodynamic metrics were used to quantify the discrepancies between the various velocity profiles. These metrics include indexed power loss (iPL), indexed viscous dissipation rate (iVDR), hepatic fluid distribution (HFD), and wall shear stress (WSS).

In the simulations, HFD was defined by the percentage of IVC flow to the LPA. The WSS parameter of interest was the percentage of TCPC surface area which experienced a WSS lower than 0.4 Pa[11, 36], denoted by $\text{A}_{\text{WSS}<0.4\text{Pa}}$. Power loss was defined by performing an energy analysis of the TCPC, modeling it as a control volume:

$$\text{PL} = \int_{CS}\left[\left(p + \frac{1}{2}\rho U^2\right)\vec{U} \bullet \vec{n}\, dA\right] \tag{5}$$

where $p, \rho, U, Q, A,$ and n are static pressure, density, velocity magnitude, flow rate, area, and the normal vector, respectively. CS indicates a control surface, which, in this case, includes the surfaces of the original vessel ends and the TCPC wall. Viscous dissipation rate, a good surrogate of PL [32], was defined as:

$$\text{VDR} = \mu_{eff}\left\{ \begin{array}{l} 2\left(\dfrac{\partial U_x}{\partial x}\right)^2 + \left(\dfrac{\partial U_x}{\partial y} + \dfrac{\partial U_y}{\partial x}\right)^2 + 2\left(\dfrac{\partial U_y}{\partial y}\right)^2 \\ + \left(\dfrac{\partial U_y}{\partial z} + \dfrac{\partial U_z}{\partial y}\right)^2 + 2\left(\dfrac{\partial U_z}{\partial z}\right)^2 + \left(\dfrac{\partial U_z}{\partial x} + \dfrac{\partial U_x}{\partial z}\right)^2 \end{array} \right\} \tag{6}$$

Indexed power loss (iPL) and indexed viscous dissipation rate (iVDR) were defined as follows:

$$\text{iPL} = \frac{\text{PL}_{\text{avg}}}{\rho Q_{s,avg}{}^3/\text{BSA}^2} \quad \& \quad \text{iVDR} = \frac{\left(\int_{Vol} \text{VDR}\,dVol\right)_{\text{avg}}}{\rho Q_{s,avg}{}^3/\text{BSA}^2} \tag{7}$$

where $Q_{s,avg}$ is time-averaged systemic venous flow, BSA is body surface area, and Ω_{avg} is the time-averaged value of the variable Ω. In this paper, characteristic discrepancies, iPL, iVDR, HFD, and $\text{A}_{\text{WSS}<0.4\text{Pa}}$, were defined to quantify the differences between the three artificial velocity profiles and the real velocity profile. Their equations are:

$$\Delta iPL_\theta = \frac{\left|iPL_\theta - iPL_r\right|}{iPL_r}(\%) \tag{8}$$

$$\Delta iVDR_\theta = \frac{\left|iVDR_\theta - iVDR_r\right|}{iVDR_r}(\%) \tag{9}$$

$$\Delta HFD_\theta = \left|HFD_\theta - HFD_r\right|(\%) \tag{10}$$

$$\Delta A_{WSS < 0.4Pa, \theta} = \left|A_{WSS < 0.4Pa, \theta} - A_{WSS < 0.4Pa, r}\right|(\%) \tag{11}$$

where θ can be either "f" for flat, "p" for parabolic, "w" for Womersley, or "e" for extension-developed profiles. It is worth noting that HFD and $A_{WSS<0.4Pa}$ are percentages by definition. Therefore, Eqs. (10) and (11) report the differences without further normalization by the value from the real velocity profile.

Furthermore, the pulsatility index, PI[33], and Womersley number, α[26], are important fluid dynamic parameters that describe pulsatile flow waveforms. They are defined as

$$PI = \frac{Q_{max} - Q_{min}}{2 \times Q_{avg}} \times 100\% \tag{12}$$

where Q_{max}, Q_{min}, and Q_{avg}, are the maximum, minimum, and time-averaged flow rates within the vessel during one cardiac cycle, respectively, and

$$\alpha = R\sqrt{\omega/\upsilon} \tag{13}$$

where R is the radius of the vessel, ω is the frequency of the flow waveform, and ν is kinematic viscosity.

Instantaneous flow eccentricity (ε_U) was obtained from the real velocity profile based on the following equation [21]:

$$\varepsilon_U = \frac{\sum_i r_i \left|\left(\overrightarrow{U} \bullet \overrightarrow{n}\right)_i\right|}{\sum_i \left|\left(\overrightarrow{U} \bullet \overrightarrow{n}\right)_i\right|} \tag{14}$$

where i is the index that loops through all lumen pixels of the actual velocity profile, and r_i is the radius of the lumen pixel in terms of the centroid of the vessel. The time-averaged flow eccentricity and its corresponding fluctuation (pulsatility) over a cardiac cycle, $\varepsilon_{U,avg}$ and $\varepsilon_{U,PI}$ respectively, were calculated.

Flow-weighted quantities were calculated based on

$$w\Pi = \sum_{i=\text{all inlets}} \Pi_i \times \frac{Q_{avg,i}}{\sum_{k=\text{all inlets}} Q_{avg,k}} \tag{15}$$

where Π can be α, PI, $\varepsilon_{U,avg}$, $\varepsilon_{U,PI}$, or nRMSD$_{avg}$ in this study.

2.6 Statistics

IBM SPSS Statistics (IBM, Inc., Aramark, NY) was utilized for statistical analysis. Significant differences were examined using a Repeated Measures ANOVA test. Because of the violation of the assumption of sphericity, the Greenhouse-Geisser correction was used to determine the existence of significant differences between different velocity profiles. Pairwise comparisons were then conducted to detect significant difference between each of the two velocity profiles. Additionally, the multiple linear regression model was used with a forward stepwise procedure. $P < 0.05$ was considered a statistically significant correlation.

3 Results

3.1 Patient Cohort

Patient demographic and hemodynamic details are provided in Table I.

3.2 Velocity Profile Comparisons

A qualitative comparison between the four velocity profile BCs for one sample case is shown in Figure 3.

The time-averaged normalized RMSD values for the comparison of the flat, parabolic, Womersley, and extension-developed velocity profiles to the real, patient-specific profile, nRMSD$_{avg,f}$, nRMSD$_{avg,p}$, nRMSD$_{avg,w}$, and nRMSD$_{avg,e}$ respectively, are given in Table II. This analysis was performed on both the IVC and SVC inlet velocity profiles. The flow-weighted nRMSD$_{avg}$ values for the flat, parabolic, Womersley, and extension-developed velocity profiles are 57.2±6.7%, 57.5±10.6%, 57.8±10.5%, and 58.2±10.8%, respectively.

3.3 Hemodynamic Results

Figure 4 and Figure 5 illustrate differences in VDR and regions of low WSS, respectively, between the various velocity profiles.

Statistical analysis of the hemodynamic metrics resulting from the five velocity profiles is summarized in Figure 6. Statistical significant differences were observed between simulations using the flat and real velocity profiles with regard to iPL ($p = 0.018$) and iVDR ($p = 0.02$), but not regarding HFD ($p = 0.77$) nor $A_{WSS<0.4Pa}$ ($p = 0.63$). No significant difference was detected between simulations using the real velocity profiles and the other three artificial velocity profiles. Additionally, four characteristic discrepancies were calculated by comparing the hemodynamic metrics from the real velocity profiles to those resulting from either the flat, parabolic, Womersley, or extension-developed profiles.

Figure 7 demonstrates that iPL and iVDR for the flat velocity profile exhibit significant differences compared to those of the parabolic ($p = 0.009$ and 0.0123, respectively),

Womersley (p = 0.004 and 0.006, respectively), and extension-developed (p = 0.038 and 0.049, respectively) velocity profiles. No significance was observed between the flat velocity profiles and the other three velocity profiles in terms of ΔHFD and ΔWSS, nor between the latter three velocity profiles regarding any characteristic discrepancies.

Furthermore, multiple linear regression analyses were conducted to explore possible correlations between the four characteristic discrepancies and flow parameters: $nRMSD_{avg,f}$, $nRMSD_{avg,p}$ $nRMSD_{avg,w}$, $nRMSD_{avg,e}$, PI_{IVC}, PI_{SVC}, a, $\varepsilon_{U,avg}$, and $\varepsilon_{U,PI}$. Correlations were found between $\varepsilon_{U,avg}$ and ΔiPL, ΔiVDR, and Δ$A_{WSS<0.4Pa}$ from simulations using the flat and extension-developed velocity profiles, as shown in Figure 8.

4 Discussion

This study is the first to investigate the effects of inlet velocity profiles on clinically important hemodynamic metrics for Fontan patients. Nine patients were involved in the study. The two major parameters that characterize the error between the input velocity profiles are ε_U and $nRSMD_{avg}$. Four characteristic discrepancies, ΔiPL, ΔHFD, ΔiVDR, and Δ$A_{WSS<0.4Pa}$, are the primary variables that quantify the difference between the real velocity profile and four artificial velocity profiles (flat, parabolic, Womersley, and extension-developed).

Qualitative differences were observed in the detailed flow fields between simulations using the patient-specific, real velocity profiles and all four artificial velocity profiles. However, statistical significance was only detected in differences in iPL and iVDR between simulations using the real and the flat velocity profiles. The characteristic discrepancies of these two hemodynamic metrics (ΔiPL and ΔiVDR) with regard to the flat velocity profile were also significantly higher than the characteristic discrepancies of the other three artificial velocity profiles. It is interesting to note that the flat profile has a similar $nRSMD_{avg}$ compared to the other three artificial profiles, and correlations were detected between $\varepsilon_{U,avg}$ and both ΔiPL$_f$ and ΔiVDR$_f$ for the flat velocity profile. Considering that both parabolic and Womersley profiles have a velocity peak at the center of the vessel, the difference in this peak between these two profiles and the real profile is exactly equal to $\varepsilon_{U,avg}$ (13.2±3.2%). However, since the flat profile does not have a spatial velocity peak, it can be assumed to be found at the boundary of the vessel. Then, the peak difference between the flat and real profiles becomes ~87%. Although the peak velocity of an extension-developed profile may not be at the center of the vessel, the peak difference between the flat and real profiles may be less than the difference between the parabolic/Womersley and real profiles, a good example of which is shown in Figure 3. Therefore, the lack of a spatial peak on the flat velocity profile may be the primary reason for its significant difference with other artificial velocity profiles when compared to the use of the real velocity profile.

A better option of artificial velocity profile that could obtain acceptable iPL and iVDR can be chosen from the other three profiles (parabolic, Womersley, and extension-developed), since no statistically significant differences were observed in these two hemodynamic metrics between simulations using these three options and the real velocity profile. Additionally, no statistical differences were found between simulations employing these

three artificial velocity profiles themselves. The reason that no statistical differences were found for all hemodynamic metrics is primarily because *these metrics are bulk hemodynamic metrics calculated throughout the TCPC volume*. The exponential decay of the error with the distance away from the boundaries may diminish the effects of the discrepancies of ~13% of ε_U and ~50% of $nRSMD_{avg}$ from the boundary conditions[29], but the errors still impact small regions in the vicinity of the boundaries, as shown in Figure 5. Furthermore, a collision between flows from the IVC and SVC may further weaken the effects of the inlet boundaries on the bulk flow field within the TCPC. Therefore, the effects of discrepancies in flow boundary profiles do not considerably influence the iPL and iVDR, as these hemodynamic metrics are affected primarily by bulk flow.

This theory may be applicable to HFD as well. Because no significant difference was observed between simulations with all four artificial velocity profiles and the real, patient-specific profile, HFD can be concluded to be even less sensitive to inlet boundary conditions than iPL and iVDR. Wall shear stress, on the other hand, is a fluid dynamic parameter that is sensitive to the choice of velocity profile [14]; therefore, the contours for regions of the TCPC wall where WSS<0.4 Pa (Figure 5) illustrate noticeable differences near the TCPC inlet boundaries. However, the effects of this difference near the boundaries may be diminished in the calculation of $A_{WSS<0.4Pa}$, since it is also a bulk metric that considers the WSS over the entirety of the TCPC wall. Nevertheless, the flat velocity profile is not recommended for assessing $A_{WSS<0.4Pa}$ because of the noticeable difference in location of the low WSS regions between the flat and real velocity profiles, as shown in Figure 5.

Moreover, it is interesting to observe that using either the parabolic or Womersley velocity profiles results in no significant difference when compared to the use of the extension-developed profile. Extension-developed profiles are generally utilized under the hypothesis that the flow loses its dependence on the inflow profile in the extensions before entering the region of interest. The development of the flow depends on the shape of the extension. In TCPC simulations, the IVC flow is typically a confluence of flow from the hepatic veins (HVs) and the IVC under the diaphragm (IVC* in Figure 2). This mixed flow travels only a short distance before reaching the plane where the IVC flow is acquired for TCPC simulations. Therefore, a long extension implemented in these simulations is ultimately unnecessary for inlet BCs. In other words, the extension-developed profile does not show any superiority to the parabolic profile in its approximation of *in vivo* flow characteristics for Fontan simulations. This theory also applies to SVC flow, which merges with flow from the innominate vein (IV).

The results of this study suggest that parabolic velocity profiles as inlet BCs are acceptable surrogates for patient-specific profiles in Fontan CFD simulations. No significant difference was observed between simulations using this profile and the real, patient-specific profile for all clinically relevant hemodynamics metrics, and characteristic discrepancies of these metrics with regard to the parabolic velocity profile were the lowest when compared to the other three artificial velocity profiles. Additionally, it is worth recalling that the enlarged domain when including flow extensions introduces an additional computational burden. Avoiding flow-extensions could reduce the computational mesh by approximately 20%, saving computational resources and decreasing simulation time. Image processing and

implementation of the real velocity profile are also not trivial and could potentially increase "segmentation processing" of "total user input time" for Fontan surgical planning[27]. While it is evident that parabolic profiles do not require these additional costs, the present study shows that for the clinical indexes of interest, they do not impair the reliability of the results. Therefore, using parabolic velocity profiles may help researchers meet the tight clinical turn-around time for Fontan surgical planning cases[27]. The better applicability of a parabolic velocity profile relies on its simplicity. First, many commercial CFD solvers have built-in subroutines to implement parabolic velocity profiles, whereas Womersley and real profiles require further development for most commercial and academic computational packages. Second, the real, patient-specific velocity profile is not always readily available, such as in the case of patients who cannot tolerate routine MRI due to implanted devices. When this is the case, echo-Doppler or catheterization becomes the routinely used alternative medical imaging technique to acquire blood flows for this patient cohort. These two techniques can only provide flow rates rather than velocity profiles. Therefore, using the real velocity profile becomes unfeasible, and the flow rate based parabolic velocity profile becomes the superior choice.

Furthermore, real, patient-specific profiles are not necessary for Fontan surgical planning. In particular, surgical planning may rely on the combination of 3D CFD simulations coupled with surrogate models represented by lumped parameter networks (LPNs)[20]. As a surrogate, LPNs incorporate patient-specific flow rates and spatially averaged pressures, as they do not have the space-dependence to incorporate velocity profiles.

However, it is worth noting that despite the aforementioned advantages of parabolic velocity profiles over real velocity profiles, the use of real velocity profiles may be essential when the location of low WSS regions is of interest, consistent with previous literature [14]. Though Figure 6 and Figure 7 show no statistically significant differences between the real and four artificial velocity profiles regarding WSS, Figure 5 illustrates slight differences in the locations of low WSS regions. Therefore, it is suggested to consider the real velocity profile in TCPC simulations used to identify low WSS regions when attempting to avoid blood clots.

The authors acknowledge that this study is based on a small cohort of Fontan patients. Though special efforts were made to cover a range of possible cardiac outputs and flow pulsatilities, a large-cohort study is needed for more generalizable results. In addition, while the hemodynamic metrics investigated in this study showed no significant differences between velocity profiles, other metrics may not follow this trend. The rigid vessel wall assumption was utilized for all simulations, considering the negligible impact of compliant vessel walls on the energy loss and HFD involved in this study[10, 25]. Long *et al.*[10] showed the effect of wall compliance on high WSS, i.e. WSS > 2 Pa, and negligible effects on low WSS in Fontan simulations. Therefore, the WSS-related findings (regarding the locations and areas experiencing low WSS) in this study may not be affected by this assumption, but a thorough investigation regarding this matter is merited.

Additionally, strictly speaking, the prescription of flow rate conditions to the incompressible Naiver-Stokes equations is a "defective" problem, as not all the data are provided for the

mathematical theory[20]. Different sophisticated mathematical approaches have been proposed in the literature to address this problem without prescribing any specific profile[6, 19, 29, 30]. However, all these approaches are computationally demanding and require non-standard customization of the numerical solvers. Therefore, they do not fit well with the purpose of the present research, which is oriented to provide practical recommendations. With the same point of view, the authors note that the parabolic and Womersley profiles considered in this study are the exact analytical solution of the incompressible Naiver-Stokes equations under many assumptions, including the Newtonian rheology. Other models, e.g. an analytical solution for an Oldroyd-B non-Newtonian rheology[13], are available, but they are less popular and add significant mathematical complexities and computational costs, while this study is to suggest a practical approach among the most used ones and to assess their practical reliability. For this reason, these complicated models are not involved in this study. Also, the parabolic and Womersley velocity profiles, theoretically, are designed for cylindrical vessels, while the cross-sections of *in vivo* vessels are not perfectly circular. A geometric transformation could be implemented to address this concern[3].

Moreover, there are two major limitations of medical images included in this study. First, the real, patient-specific velocities were obtained from PC-MRI images, which only contain through-plane velocities, while in-plane velocity is ignored. The in-plane velocity could be important, particularly, when the PC-MRI plane is close to the anastomosis between IVC/SVC to the pulmonary arteries where they are not perpendicular to the main flow direction. Emerging MR techniques, e.g. 2D PC-MRI with three directional velocity encoding and 4D PC-MRI, can obtain in-plane velocity components; however, these imaging techniques were not the routine MRI for Fontan patients. Secondly, the patients included in this study are relatively old, and the routine PC-MRI was usually acquired under breath-held conditions. Consequently, the effects of respiration on the inlet boundary profiles were not included. Respiration increases flow pulsatilities but not time-averaged flow rates[31]. Though small differences were observed in hemodynamic metrics between simulations using breath-held and respiratory inflow boundary conditions[23, 28], these differences were not reported to be statistically significant[23]. Nevertheless, the in-plane velocity components and respiration may affect the details of the flow, e.g. locations of the regions with low WSS; hence their effect on the boundary velocity profiles warrant future examinations.

In conclusion, this study is the first, to date, to investigate the effects of inlet velocity profiles on Fontan hemodynamics obtained from CFD simulations. Five types of inlet velocity profiles were involved: the real, patient-specific velocity profile and four artificial velocity profiles (flat, parabolic, Womersley, and extension-developed), which are derived from time-varying patient-specific flow rates acquired from PC-MRI. This work focused on investigating the differences in clinically relevant hemodynamic metrics, iPL, iVDR, HFD, and $A_{WSS<0.4Pa}$, between simulations employing these velocity profiles as inlet BCs. Statistical analysis showed that significant differences existed only between the use of the real velocity profile and the flat velocity profile, but not with the use of the other three artificial velocity profiles. Characteristic discrepancies for all hemodynamic metrics for using the parabolic velocity profile always exhibit the lowest cohort-averaged values compared to those for the other artificial velocity profiles. These findings suggest that the parabolic, Womersley, and extension-developed velocity profiles are acceptable surrogates

for real, patient-specific velocity profiles in Fontan simulations. But, the parabolic profile is recommended primarily because its lowest discrepancies to the real, patient-specific velocity profiles and computational cost, as well as its good robustness for more applications.

Acknowledgments

6 References

1. Arbia G, Vignon-Clementel I, Hsia TY and Gerbeau J-F. Modified Navier-Stokes equations for the outflow boundary conditions in hemodynamics. Hal-01328501 60: 175–188, 2016.

2. Bertoglio C, Caiazzo A, Bazilevs Y, Braack M, Esmaily M, Gravemeier V, A LM, Pironneau O, I EV-C and W AW. Benchmark problems for numerical treatment of backflow at open boundaries. Int J Numer Method Biomed Eng 34: 2018.

3. Boutsianis E, Gupta S, Boomsma K and Poulikakos D. Boundary conditions by Schwarz-Christoffel mapping in anatomically accurate hemodynamics. Ann Biomed Eng 36: 2068–2084, 2008. [PubMed: 18836834]

4. Campbell IC, Ries J, Dhawan SS, Quyyumi A. a., Taylor WR and Oshinski JN. Effect of Inlet Velocity Profiles on Patient-Specific Computational Fluid Dynamics Simulations of the Carotid Bifurcation. Journal of Biomechanical Engineering 134: 051001–051001, 2012. [PubMed: 22757489]

5. Cheng AL, Takao CM, Wenby RB, Meiselman HJ, Wood JC and Detterich JA. Elevated Low-Shear Blood Viscosity is Associated with Decreased Pulmonary Blood Flow in Children with Univentricular Heart Defects. Pediatric cardiology 37: 789–801, 2016. [PubMed: 26888364]

6. Formaggia L, Gerbeau JF, Nobile F and Quarteroni A. Numerical treatment of defective boundary conditions for the Navier-Stokes equations. Siam Journal on Numerical Analysis 40: 376–401, 2002.

7. Hardman D, Semple SI, Richards JMJ and Hoskins PR. Comparison of patient-specific inlet boundary conditions in the numerical modelling of blood flow in abdominal aortic aneurysm disease. International Journal for Numerical Methods in Biomedical Engineering 29: 165–178, 2013. [PubMed: 23225751]

8. Jansen IGH, Schneiders JJ, Potters WV, Van Ooij P, Van Den Berg R, Van Bavel E, Marquering HA and Majoie CBLM. Generalized versus patient-specific inflow boundary conditions in computational fluid dynamics simulations of cerebral aneurysmal hemodynamics. American Journal of Neuroradiology 35: 1543–1548, 2014. [PubMed: 24651816]

9. Khiabani RH, Whitehead KK, Han D, Restrepo M, Tang E, Bethel J, Paridon SM, Fogel M. a. and Yoganathan AP. Exercise capacity in single-ventricle patients after Fontan correlates with haemodynamic energy loss in TCPC. Heart 101: 139–143, 2015. [PubMed: 25184826]

10. Long CC, Hsu M. C. C. M. c., Bazilevs Y, Feinstein JA and Marsden AL. Fluid – structure interaction simulations of the Fontan procedure using variable wall properties. International Journal for Numerical Methods in Biomedical Engineering 28: 513–527, 2012. [PubMed: 25099455]

11. Malek AM, Alper SL and Izumo S. Hemodynamic shear stress and its role in atherosclerosis. Jama 282: 2035–2042, 1999. [PubMed: 10591386]

12. Marzo A, Singh P, Larrabide I, Radaelli A, Coley S, Gwilliam M, Wilkinson ID, Lawford P, Reymond P, Patel U, Frangi A and Hose DR. Computational hemodynamics in cerebral aneurysms: The effects of modeled versus measured boundary conditions. Annals of biomedical engineering 39: 884–896, 2011. [PubMed: 20972626]

13. McGinty S, McKee S and McDermott R. Analytic solutions of Newtonian and non-Newtonian pipe flows subject to a general time-dependent pressure gradient. Journal of Non-Newtonian Fluid Mechanics 162: 54–77, 2009.

14. Morbiducci U, Ponzini R, Gallo D, Bignardi C and Rizzo G. Inflow boundary conditions for image-based computational hemodynamics: Impact of idealized versus measured velocity profiles in the human aorta. Journal of Biomechanics 46: 102–109, 2013. [PubMed: 23159094]

15. Pandurangi UM, Shah MJ, Murali R and Cherian KM. Rapid Onset of Pulmonary Arteriovenous Malformations After Cavopulmonary Anastomosis. Ann Thorac Surg 237–239, 1999. [PubMed: 10421150]

16. Pant S, Fabrèges B, Gerbeau JF and Vignon-Clementel IE. A methodological paradigm for patient-specific multi-scale CFD simulations: From clinical measurements to parameter estimates for individual analysis. International Journal for Numerical Methods in Biomedical Engineering 30: 1614–1648, 2014. [PubMed: 25345820]

17. Pekkan K, Z??licourt DD, Ge L, Sotiropoulos F, Frakes D, Fogel MA and Yoganathan AP. Physics-driven CFD modeling of complex anatomical cardiovascular flows - A TCPC case study. Annals of biomedical engineering 33: 284–300, 2005. [PubMed: 15868719]

18. Piskin S and Serdar Celebi M. Analysis of the effects of different pulsatile inlet profiles on the hemodynamical properties of blood flow in patient specific carotid artery with stenosis. Computers in biology and medicine 43: 717–728, 2013. [PubMed: 23668347]

19. Ponzini R, Vergara C, Redaelli A and Veneziani A. Reliable CFD-based estimation of flow rate in haemodynamics measures. Ultrasound in Medicine and Biology 32: 1545–1555, 2006. [PubMed: 17045876]

20. Quarteroni A, Veneziani A and Vergara C. Geometric multiscale modeling of the cardiovascular system, between theory and practice. Computer Methods in Applied Mechanics and Engineering 302: 193–252, 2016.

21. Raghav V, Barker AJ, Mangiameli D, Mirabella L, Markl M and Yoganathan AP. Valve mediated hemodynamics and their association with distal ascending aortic diameter in bicuspid aortic valve subjects. J Magn Reson Imaging 47: 246–254, 2018. [PubMed: 28390180]

22. Srivastava D, Preminger T, Lock JE, Mandell V, Keane JF, Mayer JE, Kozakewich H and Spevak PJ. Hepatic venous blood and development of pulmonary arteriovenous malformation in congenital heart disease. Circulation 92: 1217–1222, 1995. [PubMed: 7648668]

23. Tang E, Wei ZA, Trusty PM, Whitehead KK, Mirabella L, Veneziani A, Fogel MA and Yoganathan AP. The effect of respiration-driven flow waveforms on hemodynamic metrics used in Fontan surgical planning. Journal of Biomechanics 82: 87–95, 2019. [PubMed: 30414631]

24. Tang E, Wei ZA, Whitehead KK, Khiabani RH, Restrepo M, Mirabella L, Bethel J, Paridon SM, Marino BS, Fogel MA and Yoganathan AP. Effect of Fontan geometry on exercise haemodynamics and its potential implications. Heart 103: 1806–1812, 2017. [PubMed: 28522658]

25. Tang TLE Effect of Geometry, Respiration and Vessel Deformability on Fontan Hemodynamics: a Numerical Investigation. Georgia Institute of Technology, 2015.

26. Taylor C. a., Hughes TJR and Zarins CK. Finite element modeling of blood flow in arteries. Computer Methods in Applied Mechanics and Engineering 158: 155–196, 1998.

27. Trusty PM, Slesnick TC, Wei ZA, Rossignac J, Kanter KR, Fogel MA and Yoganathan AP. Fontan Surgical Planning: Previous Accomplishments, Current Challenges, and Future Directions. J Cardiovasc Transl Res 11: 133–144, 2018. [PubMed: 29340873]

28. Van De Bruaene A, Claessen G, La Gerche A, Kung E, Marsden A, De Meester P, Devroe S, Bogaert J, Claus P, Heidbuchel H, Budts W and Gewillig M. Effect of respiration on cardiac filling at rest and during exercise in Fontan patients: A clinical and computational modeling study. IJC Heart and Vasculature 9: 100–108, 2015. [PubMed: 28785717]

29. Veneziani A and Vergara C. An approximate method for solving incompressible Navier–Stokes problems with flow rate conditions. Computer Methods in Applied Mechanics and Engineering 196: 1685–1700, 2007.

30. Veneziani A and Vergara C. Flow rate defective boundary conditions in haemodynamics simulations. International Journal for Numerical Methods in Fluids 47: 803–816, 2005.

31. Wei Z, Whitehead KK, Khiabani RH, Tree M, Tang E, Paridon SM, Fogel MA and Yoganathan AP. Respiratory Effects on Fontan Circulation During Rest and Exercise Using Real-Time Cardiac Magnetic Resonance Imaging. Ann Thorac Surg 101: 1818–1825, 2016. [PubMed: 26872728]

32. Wei ZA, Tree M, Trusty PM, Wu W, Singh-Gryzbon S and Yoganathan A. The Advantages of Viscous Dissipation Rate over Simplified Power Loss as a Fontan Hemodynamic Metric. Annals of biomedical engineering 46: 404–416, 2018. [PubMed: 29094292]

33. Wei ZA, Trusty PM, Tree M, Haggerty CM, Tang E, Fogel M and Yoganathan AP. Can time-averaged flow boundary conditions be used to meet the clinical timeline for Fontan surgical planning? J Biomech 50: 172–179, 2017. [PubMed: 27855985]

34. Whitehead KK, Pekkan K, Kitajima HD, Paridon SM, Yoganathan AP and Fogel M. a.. Nonlinear Power Loss During Exercise in Single-Ventricle Patients After the Fontan: Insights From Computational Fluid Dynamics. Circulation 116: I-165-I-171, 2007.

35. Womersley. Method for the calculation of velocity, rate of flow and viscous drag in arteries when the pressure gradient is known. Physiology 127: 553–563, 1955.

36. Yang W, Chan FP, Reddy VM, Marsden AL and Feinstein JA. Flow simulations and validation for the first cohort of patients undergoing the Y-graft Fontan procedure. The Journal of thoracic and cardiovascular surgery 149: 247–255, 2015. [PubMed: 25439766]

37. Youssefi P, Gomez A, Arthurs C, Sharma R, Jahangiri M and Figueroa CA. Impact of patient-specific inflow velocity profile on hemodynamics of the thoracic aorta. Journal of Biomechanical Engineering 140: 1–14, 2018.
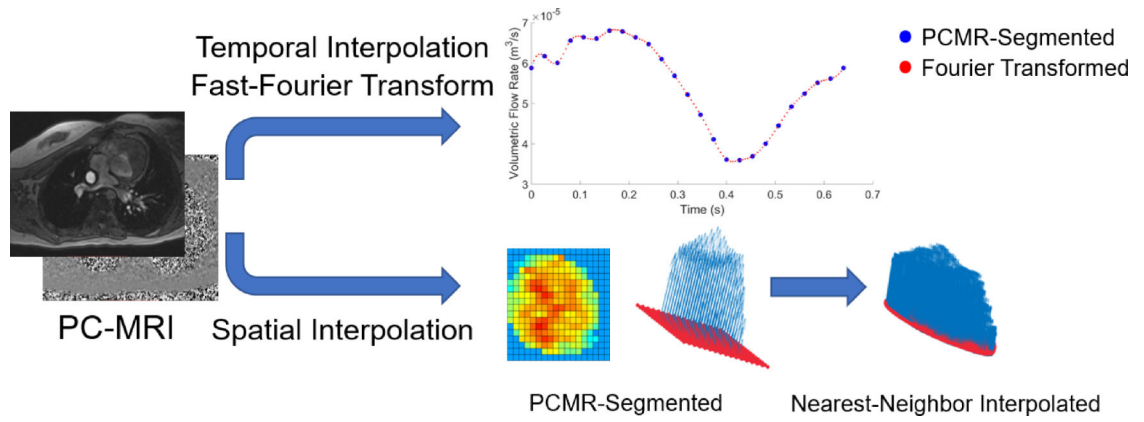
Figure 1.
Post-processing of PC-MR velocity data. Each patient's volumetric flow waveforms were temporally-interpolated with a Fast Fourier Transform, while the patient-specific velocity profiles were interpolated from the PC-MR grid to the CFD computational grid.
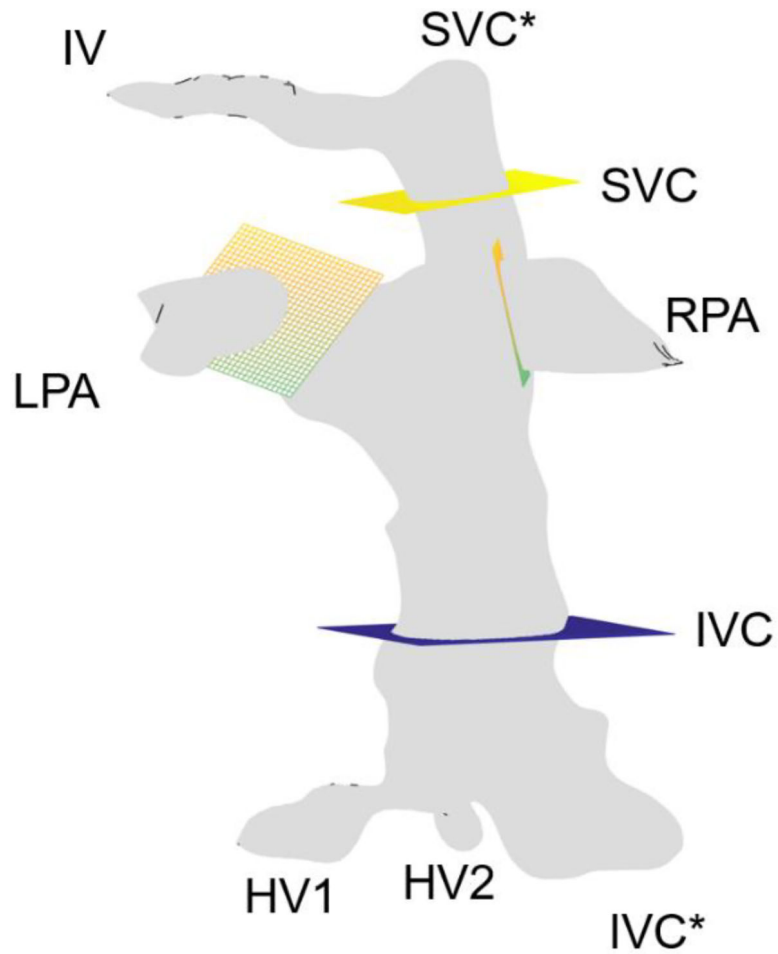
Figure 2.
Planar trimming locations on the TCPC for a sample case. Vessels were trimmed at the same location/orientation as the PC-MRI velocity planes. IVC/SVC: inferior/superior vena cava, IV: innominate vein, HV: hepatic vein, LPA/RPA: left/right pulmonary arteries, IVC*/SVC*: IVC/SVC before the confluence with HVs and IV, respectively
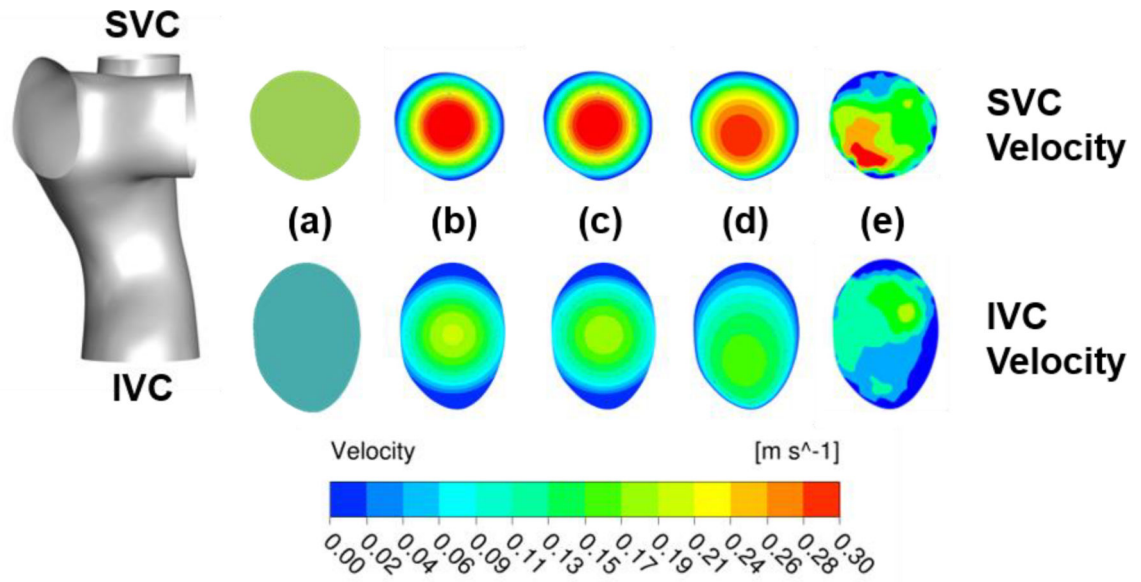
Figure 3.
A comparison of the (a) flat, (b) parabolic, (c) Womersley, (d) extension-developed, and (e) real velocity profile BCs for a sample case
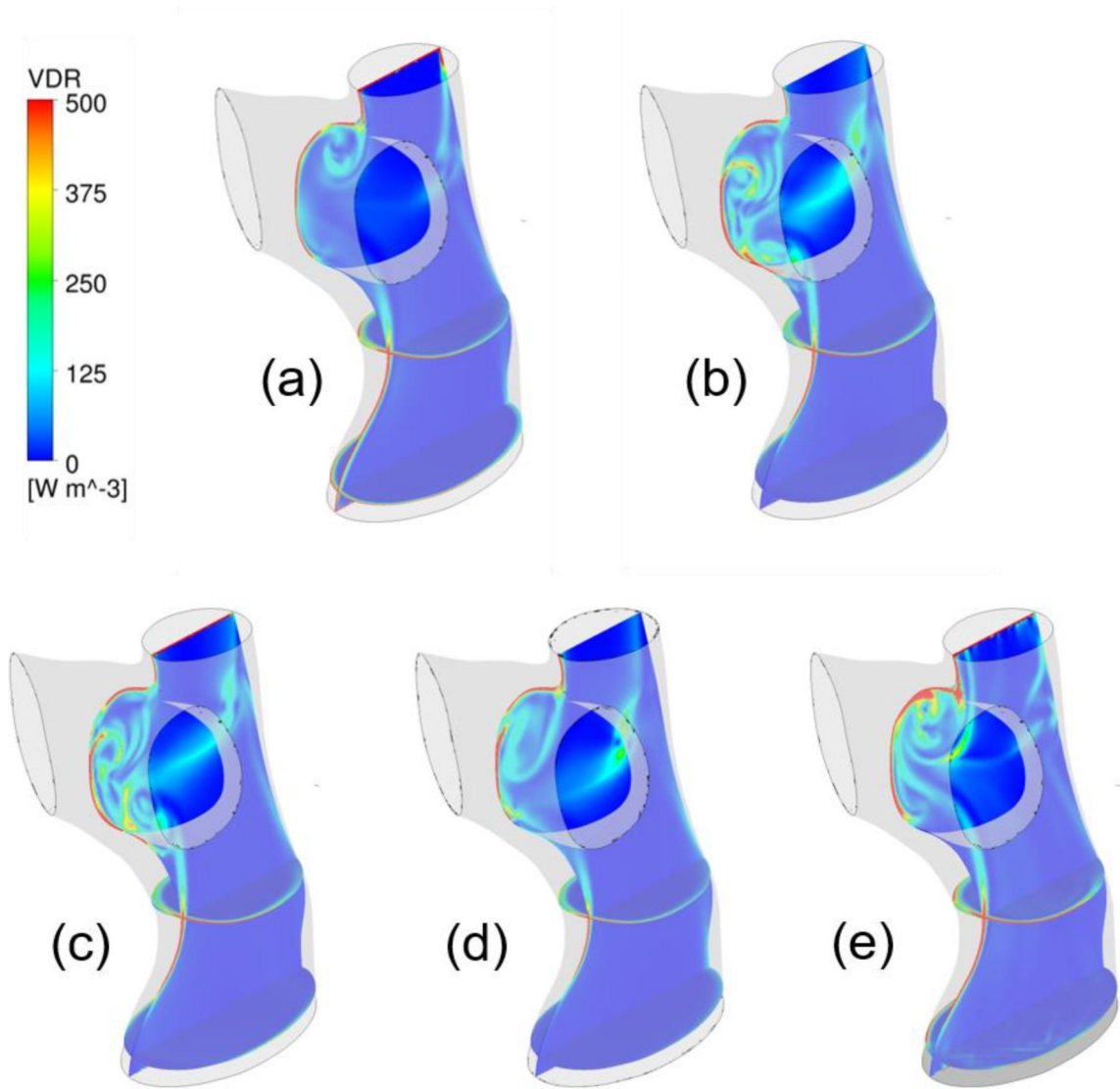
Figure 4.
Comparison of VDR in multiple planes between the (a) flat, (b) parabolic, (c) Womersley, (d) extension-developed, and (e) real velocity profile BCs for a sample case.
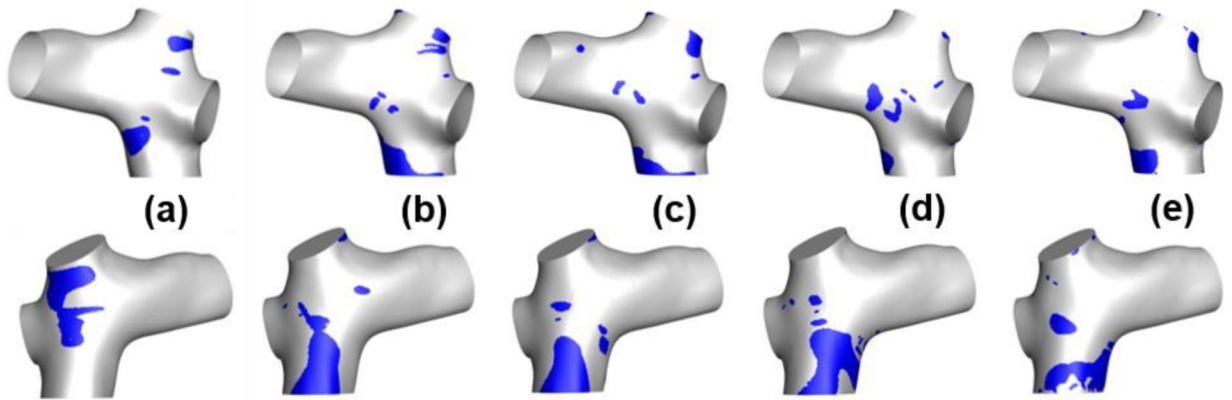
Figure 5.
Comparison of $A_{WSS<0.4Pa}$ between the (a) flat, (b) parabolic, (c) Womersley, (d) extension-developed, and (e) real velocity profile BCs for a sample case. The top row is the posterior view, and the bottom row is the anterior view.
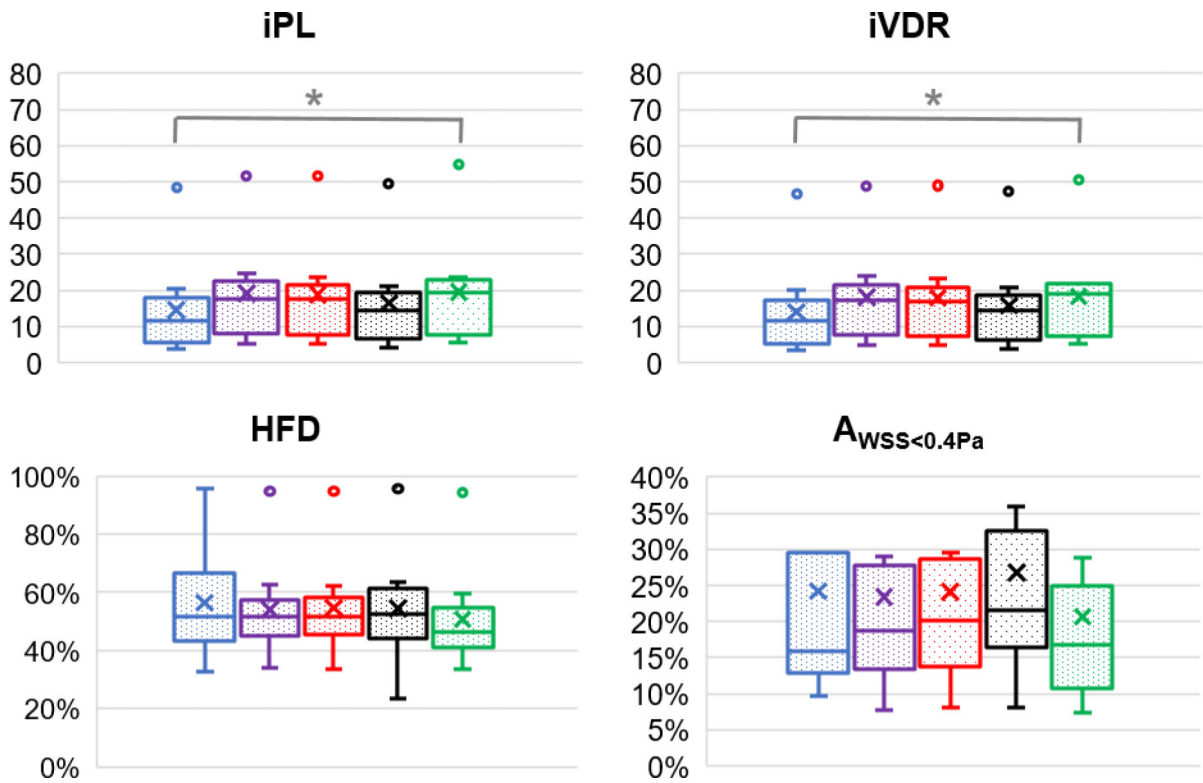
Figure 6.
Box and Whisker plots for hemodynamic metrics resulting from the flat (F, teal boxes), parabolic (P, purple boxes), Womersley (W, red boxes), extension-developed (E, black boxes), and real (R, green boxes) velocity profiles. The asterisk indicates a statistically significant difference ($p < 0.05$) between the two velocity profiles.
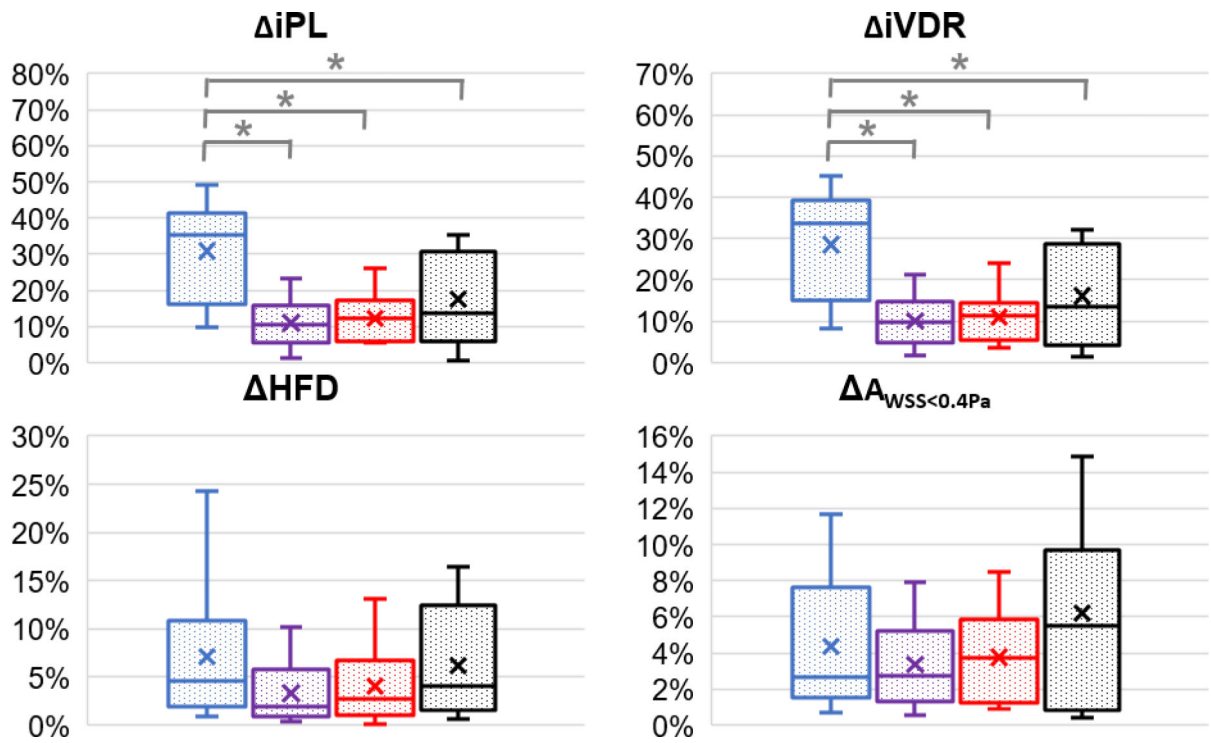
Figure 7.
Box and Whisker plots for characteristic discrepancies of hemodynamic metrics resulting from the flat (F, teal boxes), parabolic (P, purple boxes), Womersley (W, red boxes), and extension-developed (E, black boxes) velocity profiles. The asterisk indicates a statistically significant difference ($p < 0.05$) between the two velocity profiles.
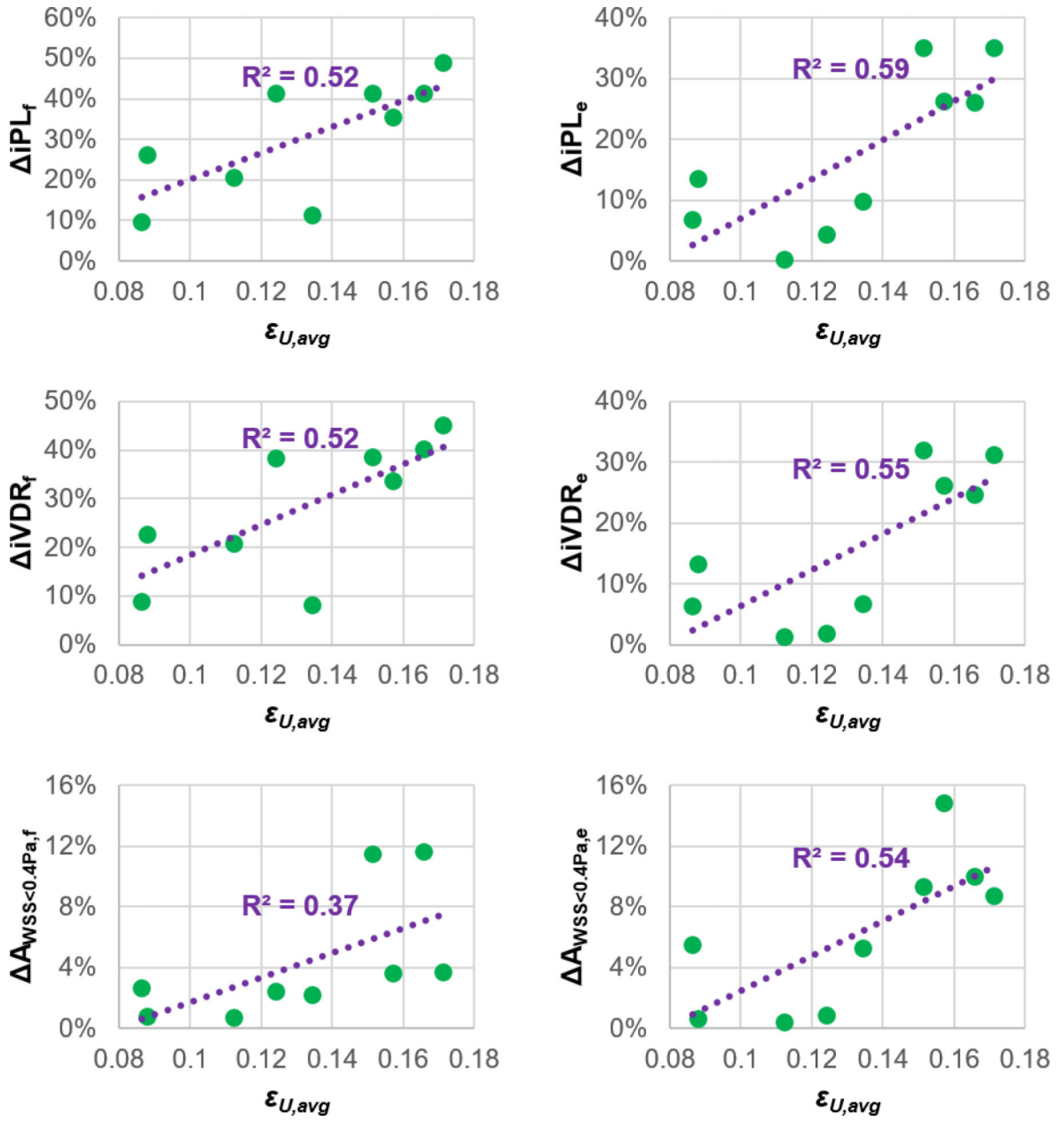
Figure 8.
Significant correlations between $\varepsilon_{U,avg}$ and ΔiPL, ΔiVDR, and Δ$A_{WSS<0.4Pa}$ from simulations using the flat and extension-developed velocity profiles.

Table I

Patient demographic and hemodynamic information (n=9)

Age (y)	13.5±5.3
BSA (m^2)	1.4±0.5
Gender (male/female)	5/4
Cardiac Output (L/min)	4.0±1.6
PI (IVC/SVC, %)	73.9±44.2/77.3±31.1
Weighted $\varepsilon_{U,avg}$ (%)	13.2±3.2
Weighted $\varepsilon_{U,PI}$	70.3±26.2
α (IVC/SVC)	15.7±3.3/11.9±1.9
Reynolds Number (IVC/SVC)	850±404/556±96

Data reported as mean±standard deviation.

Table II

Tabulated nRMSD$_{avg}$ for all patients

ID	nRMSD$_{avg,f}$		nRMSD$_{avg,p}$		nRMSD$_{avg,w}$		nRMSD$_{avg,e}$	
	IVC	SVC	IVC	SVC	IVC	SVC	IVC	SVC
1	56.1%	47.5%	41.9%	42.4%	42.1%	43.6%	44.7%	39.4%
2	44.4%	76.6%	34.9%	90.6%	35.1%	91.1%	27.0%	78.8%
3	40.4%	54.6%	42.2%	47.4%	42.4%	48.5%	71.8%	39.2%
4	52.1%	47.1%	54.2%	52.7%	54.9%	53.3%	59.9%	45.4%
5	48.5%	75.7%	43.2%	75.1%	43.2%	75.4%	35.2%	67.5%
6	65.4%	45.7%	66.9%	45.1%	67.5%	45.1%	78.0%	47.0%
7	66.4%	47.4%	62.4%	52.7%	62.6%	53.0%	79.1%	45.3%
8	57.5%	56.5%	71.0%	52.4%	71.0%	51.9%	65.4%	54.5%
9	73.5%	58.8%	81.7%	52.1%	81.8%	53.2%	80.0%	50.2%
Avg	56±10%	57±12%	55±16%	57±16%	56±16%	57±16%	60±20%	52±13%